

Article

Effects of Fe and Ni Doping on the Electronic Structure and Optical Properties of $\text{Cu}_2\text{ZnSnS}_4$

Xiufan Yang *, Xinmao Qin , Wanjun Yan, Chunhong Zhang and Dianxi Zhang

College of Physics and Electronic Science, Anshun University, Anshun 561000, China; qxm200711@126.com (X.Q.); yanwanjun7817@163.com (W.Y.); huimou1982@163.com (C.Z.); xiwa_315@163.com (D.Z.)

* Correspondence: xnmdyxf@163.com

Abstract: This study evaluated the electronic structure and optical properties of Fe-doped, Ni-doped, and (Fe,Ni)-co-doped $\text{Cu}_2\text{ZnSnS}_4$ through the first-principles pseudopotential plane-wave method based on density functional theory. The results indicated that Fe single-doping and Ni single-doping $\text{Cu}_2\text{ZnSnS}_4$ can reduce the charge transfer number of adjacent S atoms, enhancing covalent bonding in Fe–S and Ni–S bonds and reducing the bond length, lattice constants a and c , and unit cell volume v . The formation energies for Fe-doping, Ni-doping, and (Fe,Ni)-co-doping were 1.0 eV, 0.58 eV, and 0.78 eV, respectively. Both Fe and Ni-doping introduced 3d electrons near the Fermi level, resulting in new impurity levels and a gradual decrease in the band gap of $\text{Cu}_2\text{ZnSnS}_4$ from 0.16 eV. The conduction band density of $\text{Cu}_2\text{ZnSnS}_4$ was primarily contributed by Sn 5s, Sn 5p, and a portion of S 3p orbital electrons, whereas the valence band density mainly stemmed from Cu 3d, Sn 5p, and S 3p orbital electrons. Fe and Ni-doping also partly contributed to the 3d layer electrons. In the case of (Fe,Ni)-co-doping, the maximum static dielectric constant was 100.49, and the dielectric peak shifted toward the low-energy direction in the presence of both Fe and Ni. Within the visible light range, Fe-doping, Ni-doping, and (Fe,Ni)-co-doping in $\text{Cu}_2\text{ZnSnS}_4$ exhibited absorption coefficients greater than 10^4 cm^{-1} , with the maximum absorption coefficient being $1.6 \times 10^5 \text{ cm}^{-1}$ in the case of (Fe,Ni)-co-doping. In the energy range from 1.5 to 6.3 eV, the reflectivity of $\text{Cu}_2\text{ZnSnS}_4$ doped with Fe, Ni, or both was lower than 30%. Notably, a high conductivity peak at 1.9 eV indicated that $\text{Cu}_2\text{ZnSnS}_4$ possesses good photoconductivity in the visible range. Fe-doping and Ni-doping resulted in a slight shift of the conductance peak position toward the low-energy direction, accompanied by an increase in the peak value.

Keywords: $\text{Cu}_2\text{ZnSnS}_4$; Fe-doping; Ni-doping; electronic structure; optical properties; first principles



Citation: Yang, X.; Qin, X.; Yan, W.; Zhang, C.; Zhang, D. Effects of Fe and Ni Doping on the Electronic Structure and Optical Properties of $\text{Cu}_2\text{ZnSnS}_4$. *Crystals* **2023**, *13*, 1082. <https://doi.org/10.3390/cryst13071082>

Academic Editor: Duc Nguyen-Manh

Received: 6 June 2023

Revised: 5 July 2023

Accepted: 6 July 2023

Published: 11 July 2023



Copyright: © 2023 by the authors. Licensee MDPI, Basel, Switzerland. This article is an open access article distributed under the terms and conditions of the Creative Commons Attribution (CC BY) license (<https://creativecommons.org/licenses/by/4.0/>).

1. Introduction

The increasing depletion of fossil and other energy sources and the resulting energy crisis pose severe challenges to manufacturing industries and daily life. Solar energy is considered an effective solution to energy scarcity [1]. Solar energy is converted into electricity primarily using solar cells, which are conventionally silicon-based [2]. Silicon-based solar cells are primarily used in solar cell arrays, which require large surface areas and ample solar radiation [3]. However, with the improving living standards, the demand for flexible and wearable solar cells has emerged, leading to the development of thin-film solar cells [4]. Among various semiconductor materials, $\text{Cu}_2\text{ZnSnS}_4$ (CZTS) is considered the most promising material for thin-film solar cells [5]. This is attributed to its band gap falling between 1.4 and 1.6 eV and its absorption coefficient exceeding 10^4 cm^{-1} , making it highly suitable as an absorption layer in solar cells [6]. Moreover, the elements constituting $\text{Cu}_2\text{ZnSnS}_4$ are non-toxic, environmentally friendly, and abundant in the Earth's crust, making it a cost-effective and sustainable material for solar cells. Thus far, the highest conversion efficiency achieved by $\text{Cu}_2\text{ZnSnS}_4$ thin-film solar cells has been 12.6% [7], which is considerably lower than the theoretical conversion efficiency of 32.4% [8]. The

primary factors affecting the conversion efficiency of $\text{Cu}_2\text{ZnSnS}_4$ thin-film solar cells are the open circuit voltage (Voc) and low fill factor (FF) [9,10]. $\text{Cu}_2\text{ZnSnS}_4$ system exhibits a narrow phase-stability region, making it susceptible to defects due to atomic loss or substitution [11]. For example, because of the similarity in ion radii between Zn and Cu, shallow energy level defects, such as Cu_{Zn} and Zn_{Cu} substitution defects, can easily form [12]. In addition, deep-level defects, such as Sn_{Zn} substitution defects (Sn_{Zn}) and sulfur vacancy defects (V_{S}), can form within the $\text{Cu}_2\text{ZnSnS}_4$ system [13–15]. Furthermore, the system is susceptible to substitution defects, such as Zn_{Sn} , and vacancy defects, such as V_{Cu} , V_{Zn} , and V_{Sn} [16]. Studies have demonstrated that deep energy level defects or defect pairs in $\text{Cu}_2\text{ZnSnS}_4$ systems lead to the generation of tail states [17,18]. At low temperatures, tail states can capture photo-generated carriers, resulting in non-radiative recombination, which reduces the open-circuit voltage and affects the conversion efficiency of solar cells. In the case of $\text{Cu}_2\text{ZnSnS}_4$ thin-film solar cells, inhibiting the formation of deep-energy-level defects, enhancing crystal quality, and inhibiting tail states are effective approaches to improve the conversion efficiency. Previous research [19] has revealed that metal substitution doping can alter the phase structure of $\text{Cu}_2\text{ZnSnS}_4$, thereby serving as a defect passivation method. For example, various studies have incorporated metals, such as Li, Na, K, Ag, Cd, Mn, and Al, into $\text{Cu}_2\text{ZnSnS}_4$, yielding significant results [20–25]. However, studies on the elemental doping of $\text{Cu}_2\text{ZnSnS}_4$ have primarily focused on alkali metals, with limited reports on Fe and Ni-doping. Doping semiconductor materials with Fe and Ni can demonstrably enhance electrocatalytic performance, leading to considerable improvements in light absorption [26,27]. Therefore, this study analyzed the electronic structure and optical properties of $\text{Cu}_2\text{ZnSnS}_4$ doped with Fe, Ni, and their co-doping (Fe,Ni) through the pseudopotential plane-wave method based on density functional theory (DFT). The effects of Fe and Ni-doping on the structure, state density, and optical properties of $\text{Cu}_2\text{ZnSnS}_4$ bands were analyzed.

2. Theoretical Models and Calculation Methods

We used $\text{Cu}_2\text{ZnSnS}_4$ unit cells with a kesterite structure with the space group being $I\bar{4}(No.82)$. Each unit cell consisted of 4 Cu atoms, 2 Zn atoms, 2 Sn atoms, and 8 S atoms, with lattice constants of $a = 0.5428$ nm and $c = 1.0864$ nm [28]. In the calculations for single-doping and co-doping, $2 \times 1 \times 1$ superunit cells (a total of 32 atoms) were utilized. In Fe-doping, the Zn atom at the Zn 1 position of the superunit cell was substituted with an Fe atom. In Ni-doping, the Zn atom at the Zn 1 position was substituted by a Ni atom. In co-doping, the Zn atom at the Zn 1 position of the superunit cell and the Cu atom at the Cu 1 position were substituted by Fe and Ni, respectively. The doping model of the $\text{Cu}_2\text{ZnSnS}_4$ supercell is depicted in Figure 1.

The pseudopotential plane-wave method based on DFT [29,30] was adopted for calculations conducted using the CASTEP software package [31] in the Materials Studio [32] simulation platform. The Perdew–Burke–Ernzerhof (PBE) functional with generalized gradient approximation (GGA) [33] was employed to determine the exchange correlation energy between electrons. Furthermore, the interactions between real ionic and electronic states were treated using ultra-soft pseudopotentials [34]. The plane-wave truncation energy was set to 380 eV, and the self-consistent convergence accuracy was set at 5.0×10^{-7} eV/atom. The Brillouin zone integrals were divided using Monkhorst–Pack's $4 \times 4 \times 4$ scheme.

To ensure the convergence of the calculation results, a k -point convergence test was conducted within the range from $1 \times 1 \times 1$ to $7 \times 7 \times 7$. The total energy began to converge when the k -point was sampled as $4 \times 4 \times 4$. Therefore, the k -point selected for this study ensured convergence. The results of the k -point convergence test are presented in Figure 2.

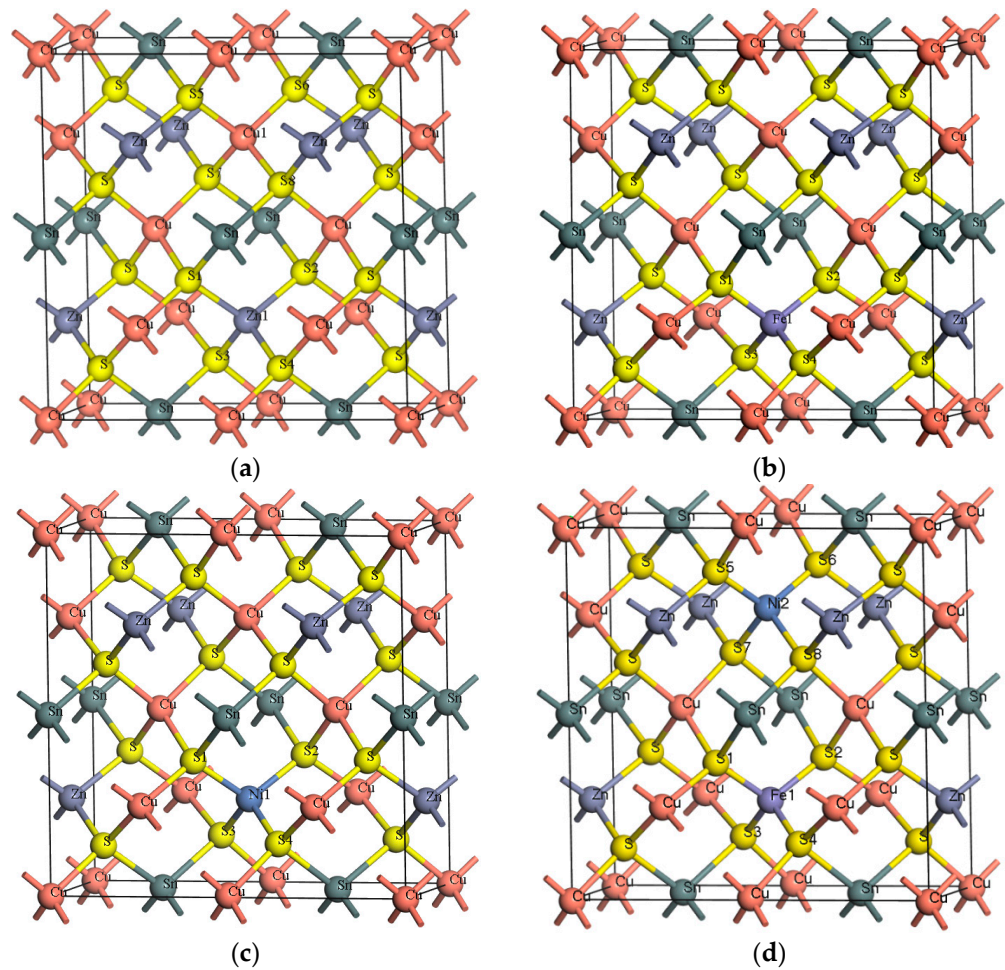


Figure 1. Structure of the single-doped and co-doped $\text{Cu}_2\text{ZnSnS}_4$ supercell: (a) $\text{Cu}_2\text{ZnSnS}_4$ supercell ($2 \times 1 \times 1$); (b) Fe-single-doping model; (c) Ni-single-doping model; (d) (Fe,Ni)-co-doping model.

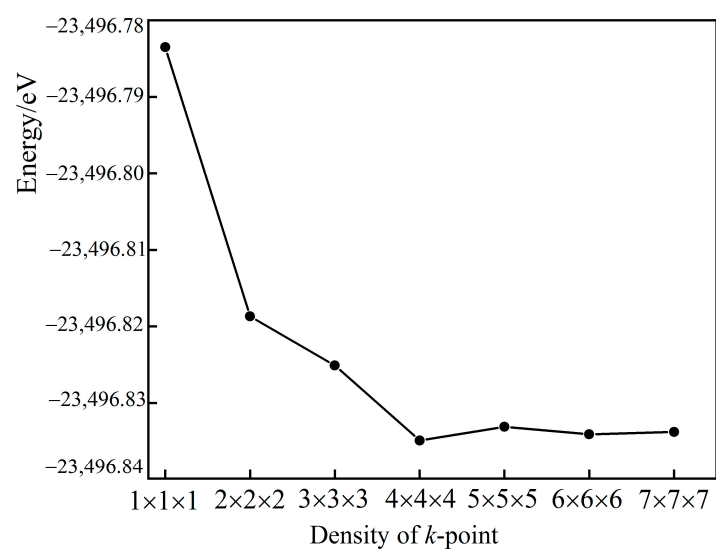


Figure 2. k -point convergence test.

To assess the feasibility of atomic doping, the doping energies of Fe and Ni atoms were calculated individually, as well as for their co-doping in $\text{Cu}_2\text{ZnSnS}_4$. The doping formation energy was calculated as follows [35,36]:

$$E(\text{Fe} \rightarrow \text{Zn})_{\text{form}} = E(\text{Fe})_{\text{doped}} - E_{\text{pure}} + \mu_{\text{Zn}} - \mu_{\text{Fe}} \quad (1)$$

$$E(\text{Ni} \rightarrow \text{Zn})_{\text{form}} = E(\text{Ni})_{\text{doped}} - E_{\text{pure}} + \mu_{\text{Zn}} - \mu_{\text{Ni}} \quad (2)$$

$$E(\text{Fe} \rightarrow \text{Zn}, \text{Ni} \rightarrow \text{Cu})_{\text{form}} = E(\text{Fe}, \text{Ni})_{\text{doped}} - E_{\text{pure}} + (\mu_{\text{Zn}} - \mu_{\text{Fe}}) + (\mu_{\text{Cu}} - \mu_{\text{Ni}}) \quad (3)$$

representing the doping formation energies of Fe-doping, Ni-doping, and (Fe,Ni)-co-doping $\text{Cu}_2\text{ZnSnS}_4$, respectively. $E(\text{Fe})_{\text{doped}}$, $E(\text{Ni})_{\text{doped}}$, $E(\text{Fe}, \text{Ni})_{\text{doped}}$ represent the energies of Fe-doping, Ni-doping, and (Fe,Ni)-co-doping $\text{Cu}_2\text{ZnSnS}_4$ after optimization, respectively. E_{pure} denotes the total energy of the undoped system of $\text{Cu}_2\text{ZnSnS}_4$. μ_{Zn} , μ_{Fe} , μ_{Ni} , and μ_{Cu} denote the chemical potential of the Zn atom, Fe atom, Ni atom, and Cu atom, respectively.

3. Results and Discussion

3.1. Geometric Structure Optimization

Table 1 presents the lattice constants and doping formation energy of undoped and doped $\text{Cu}_2\text{ZnSnS}_4$. The lattice constants a and c were compared with experimental values. As indicated by the data in Table 1, the lattice constants $a = 5.4690 \text{ \AA}$ and $c = 10.9460 \text{ \AA}$ obtained from the geometric structure optimization of $\text{Cu}_2\text{ZnSnS}_4$ are consistent with both experimental and theoretical calculations [37,38]. Both Fe and Ni doping slightly reduced the lattice constants and cell volume v of $\text{Cu}_2\text{ZnSnS}_4$. Because the ionic radii of Ni^{2+} (0.69 \AA) and Fe^{3+} (0.64 \AA) are smaller than that of Zn^{2+} (0.74 \AA) [39,40], the atomic spacing decreased upon substituting Zn atoms with Fe and Ni atoms, resulting in a decrease in lattice constants and the unit cell volume.

Table 1. Lattice constants and doping formation energy of Fe and Ni-doping in $\text{Cu}_2\text{ZnSnS}_4$.

Sample	$a/\text{\AA}$	$a\%$	$c/\text{\AA}$	$c\%$	$v/\text{\AA}^3$	Formation Energy/eV
Un-doping $\text{Cu}_2\text{ZnSnS}_4$ (experiment) [33]	5.4270	—	10.8710	—	—	—
Un-doping $\text{Cu}_2\text{ZnSnS}_4$ (calculated) [34]	5.4710	—	10.9440	—	—	—
Geometry optimization $\text{Cu}_2\text{ZnSnS}_4$	5.4690	0.77%	10.9460	0.69%	655.0330	—
Fe-doping $\text{Cu}_2\text{ZnSnS}_4$	5.4415	0.27%	10.9194	0.45%	647.9225	1.00
Ni-doping $\text{Cu}_2\text{ZnSnS}_4$	5.4460	0.35%	10.9085	0.34%	647.0102	0.58
(Fe,Ni)-co-doping $\text{Cu}_2\text{ZnSnS}_4$	5.3665	−1.11%	11.1363	2.44%	652.0260	0.78

After (Fe,Ni)-co-doping, the lattice constant a of $\text{Cu}_2\text{ZnSnS}_4$ decreased, while the lattice constant c and cell volume v increased slightly compared to those with single-doping.

As mentioned in Table 1, the formation energy of Fe-doping was 1.0 eV, whereas the formation energy of Ni-doping was 0.58 eV. Ni atoms integrated more easily into the $\text{Cu}_2\text{ZnSnS}_4$ lattice than Fe atoms. The co-doping formation energy of Fe and Ni atoms was 0.78 eV, which was lower than the formation energy of Fe-atom-doping. Under all three doping conditions, the doping formation energy was greater than 0 eV, indicating that Fe and Ni-doping defect states cannot form spontaneously, and defect states in $\text{Cu}_2\text{ZnSnS}_4$ can be controlled through co-doping.

The external electron arrangement of Fe is $3d^64s^2$, while that of Ni is $3d^84s^2$. The 3d state of Ni exhibits a denser and wider energy level than the 3d state of Fe, facilitating the capture of electrons. Upon substituting Zn, Ni tends to undergo acceptor doping [41], resulting in a lower doping formation energy. Therefore, Ni is more readily doped into $\text{Cu}_2\text{ZnSnS}_4$ than Fe. In co-doping, Fe substituted Cu. With the $3d^{10}4s^1$ electronic

arrangement outside the nucleus of Cu, the 4s layer can accept electrons. In this scenario, Fe tends to undergo donor doping [41], leading to a higher doping formation energy. Thus, inco-doping, both acceptor doping and donor doping co-occur, resulting in an intermediate doping formation energy.

3.2. Electronic Structure

3.2.1. Energy Band Structure

The high symmetry points of $\text{Cu}_2\text{ZnSnS}_4$ are G, F, Q, and Z. The coordinates of these high symmetry points are listed in Table 2.

Table 2. Coordinates of high symmetric points.

High Symmetry Point	x	y	z
G	0.000	0.000	0.000
F	0.000	0.500	0.000
Q	0.000	0.500	0.500
Z	0.000	0.000	0.500
G	0.000	0.000	0.000

Figure 3 illustrates the band structure of Fe-doping and Ni-doping in $\text{Cu}_2\text{ZnSnS}_4$. Figure 3a presents the band structure of undoped $\text{Cu}_2\text{ZnSnS}_4$, with the minimum band gap occurring at the high symmetry point G. The value of the undoped band gap was 0.16 eV, consistent with the findings of Zhao [42]. The band gap values for Fe-doped and Ni-doped $\text{Cu}_2\text{ZnSnS}_4$ were consistent with experimental values reported in the literature [43,44], indicating a decrease in the band gap values of $\text{Cu}_2\text{ZnSnS}_4$ after Fe and Ni-doping. The generalized gradient approximation (GGA) functional is a common functional used to calculate semiconductor materials, and underestimating band gap is a feature of this functional. Zhao [42] found that the band gap calculated using the GGA functional was about 1 eV lower than the experimental value. The calculated results were lower than the experimental values primarily because the DFT theoretical framework does not consider the discontinuity of the exchange correlation potential and underestimates the interaction between excited state electrons in the multi-particle system. However, this discrepancy did not affect subsequent calculations and analysis [45,46].

Figure 3b displays the energy band structure of Fe-doped $\text{Cu}_2\text{ZnSnS}_4$, Figure 3c shows the band structure of Ni-doping in $\text{Cu}_2\text{ZnSnS}_4$, and Figure 3d shows the band structure of (Fe,Ni)-co-doped $\text{Cu}_2\text{ZnSnS}_4$. It can be seen from the figure that there is almost no band gap after Fe and Ni-doping. The valence band of $\text{Cu}_2\text{ZnSnS}_4$ is mainly composed of the hybridization of Cu/Zn 3d states and S 3p states, while the conduction band is mainly composed of Sn 5s states and S 3p states. Both Fe and Ni have partially filled 3d orbitals, and these partially filled 3d orbitals have a stronger effect on the hybridization of orbital electrons. When Fe and Ni ions are doped, the 3d states of Fe and Ni are hybridized with the 3p states of S, which results in a narrower band gap [47]. In addition, after Fe or Ni-doping, the partially filled 3d orbitals reduce the s-p repulsion between Sn and S and reduce the energy of the conduction band minimum (CBM) state, thus reducing the band gap [44]. After (Fe,Ni)-co-doping, more partially filled 3d orbitals are provided, and the 3d states of Fe and Ni are hybridized more strongly with the 3p orbitals of S, the valence band moves down more, and the band gap is smaller. Considering the above factors, $\text{Cu}_2\text{ZnSnS}_4$ doped with Fe and Ni does not show a band gap. Of course, this is only the result obtained by using the GGA functional calculation, but we believe that the actual experiment has a band gap, and our calculation results can provide some new ideas for the regulating band gap of $\text{Cu}_2\text{ZnSnS}_4$.

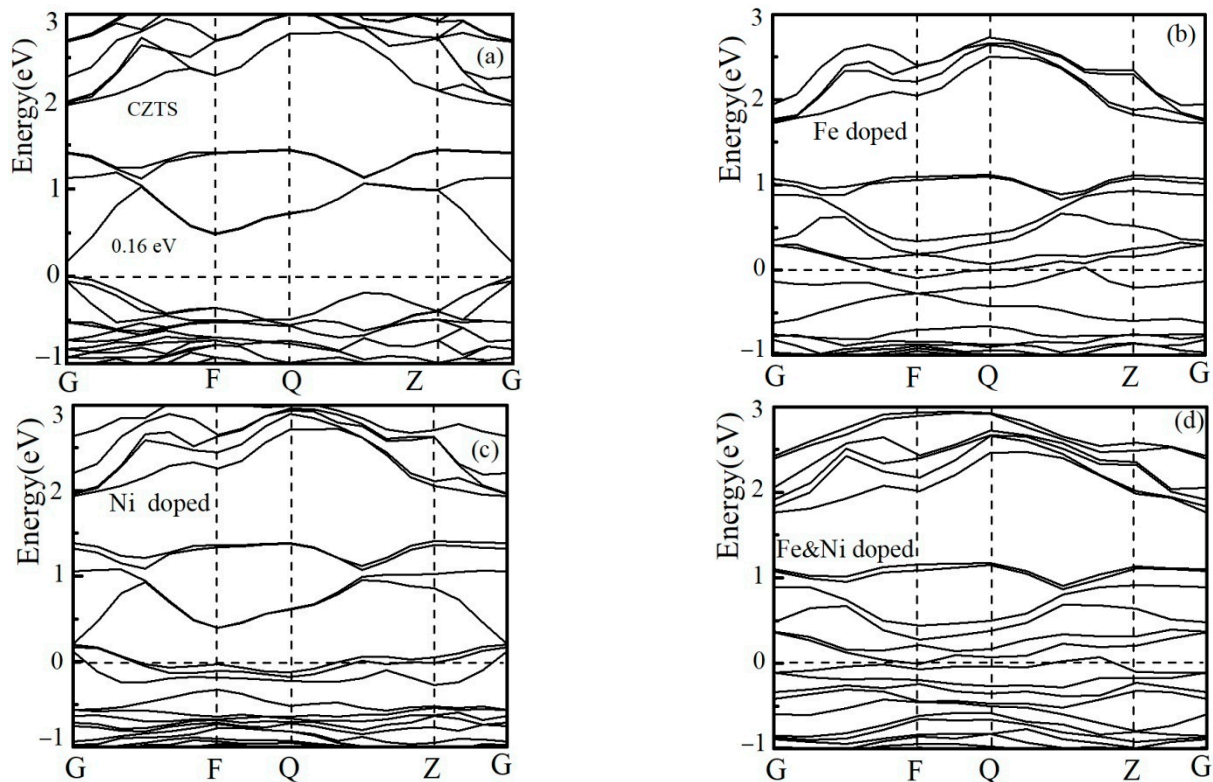


Figure 3. Band structure of Fe-doped and Ni-doped $\text{Cu}_2\text{ZnSnS}_4$: (a) undoped band structure, (b) Fe-doped band structure, (c) Ni-doped band structure, and (d) (Fe,Ni)-co-doped band structure.

3.2.2. Electronic Density of States

Figure 4 presents the total electronic density of states and the partial wave density of states for each sublayer of Fe-doping and Ni-doping $\text{Cu}_2\text{ZnSnS}_4$. Figure 4a illustrates the total electronic density of states and partial wave density of states for undoped $\text{Cu}_2\text{ZnSnS}_4$. The density of states primarily resulted from the 3d layer electrons of Cu, Zn, and S. Additionally, a few 5s and 5p layer electrons of Sn contributed to the density of states of $\text{Cu}_2\text{ZnSnS}_4$. The energy range from -14 to -12.4 eV can be primarily attributed to the 3s layer electrons of S and the 5s and 5p layer electrons of Sn. The energy range from -8.2 to -5.0 eV mainly comprises the 3s layer electrons of Zn, the 5s electrons of Sn, and the 3p layer electrons of S. The energy range from -5.0 to -0.21 eV is primarily influenced by the 3d layer electrons of Cu, the 5p layer electrons of Sn, and the 3p layer electrons of S. Lastly, the energy range from 0.6 to 3 eV is primarily associated with the electrons in the 3p layer of S and the 5s and 5p layers of Sn.

As illustrated in Figure 4b–d, all of Fe-doped, Ni-doped, and (Fe,Ni)-co-doped $\text{Cu}_2\text{ZnSnS}_4$ result in an increase in the electron state density around 0 eV. (Fe,Ni)-co-doping resulted in the highest increase of 12.9 . This increase can be attributed to the 3d electrons provided by Fe-doping or Ni-doping at approximately 0 eV. After Fe-doping, Ni-doping, or (Fe,Ni)-co-doping, the peaks of density at -12.98 eV in the lower valence band, -6.8 eV in the middle band, and -3.7 eV and -1.7 eV in the upper valence band all shifted toward lower energy levels, with an average deviation of 0.35 eV in the density of the valence band. The peaks at 1.19 eV and 2.78 eV in the conduction band also shifted toward the low-energy region, leading to an average deviation of 0.41 eV of the density of the conduction zone. These shifts in peak positions indicate that Fe-doping and Ni-doping encourage electrons in the valence band and conduction band of $\text{Cu}_2\text{ZnSnS}_4$ to occupy low-energy orbits. Moreover, the downward shift of the orbital energy level in the conduction band was greater than that in the valence band, causing the Fermi energy level to be embedded in the valence band.

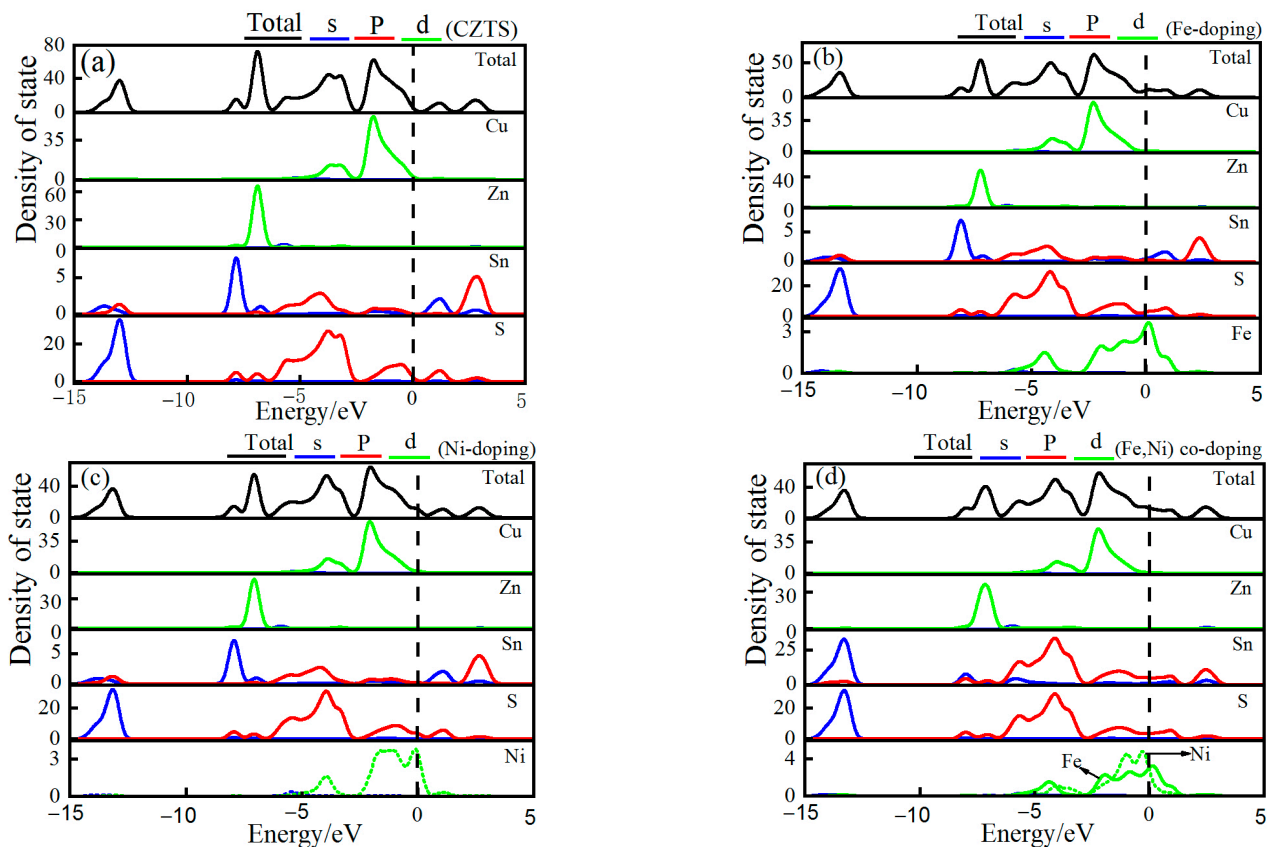


Figure 4. Electronic densities of state of Fe-doped and Ni-doped $\text{Cu}_2\text{ZnSnS}_4$. (a) Electronic density of state of undoped $\text{Cu}_2\text{ZnSnS}_4$. (b) Fe-doped $\text{Cu}_2\text{ZnSnS}_4$ electronic density of state. (c) Electronic density of state of Ni-doped $\text{Cu}_2\text{ZnSnS}_4$. (d) Electronic density of state of (Fe,Ni)-co-doped $\text{Cu}_2\text{ZnSnS}_4$.

3.3. Mulliken Population Analysis

Table 3 presents the Mulliken population analysis results for atoms adjacent to Fe and Ni impurity atoms, and Table 4 displays the Mulliken population analysis results for bonds adjacent to Fe and Ni impurity atoms. The S 1, S 2, S 3, and S 4 atoms were adjacent to the Fe 1 and Ni 1 impurity atoms, whereas the S 5, S 6, S 7, and S 8 atoms were adjacent to the Ni 2 impurity atoms. As indicated by the data in Table 3, upon replacing Zn 1 with Fe 1, the charge transfer of the S atoms adjacent to Fe 1 increased from $-0.37 e$ to $-0.24 e$ and $-0.26 e$, suggesting a weakened charge transfer due to Fe-doping. This effect can be attributed to the smaller ionic radius of Fe compared to Zn, which results in the stronger binding of charges. Conversely, upon replacing Zn 1 with Ni 1, the Ni atoms acquire a slight charge of $-0.03 e$ because the 3d shell of Ni was not completely filled with electrons, making it vulnerable to capturing charges from adjacent atoms. Simultaneously, the average charge transfer of the S atoms adjacent to Ni 1 decreased by $0.09 e$, which was influenced by the stronger binding capacity of Ni due to its smaller ionic radius compared with Zn.

After (Fe,Ni)-co-doping, the charge transfer of the S atoms adjacent to Fe 1 was consistent with that observed in single-doping scenarios. However, the charge transfer of S atoms adjacent to Ni 2 changed significantly, with an average increase of $0.05 e$ compared to single-doping. This change can be attributed to the use of Ni 2 to substitute for Cu 1 in co-doping. The smaller ionic radius of Ni resulted in a stronger binding capacity.

As indicated by the data in Table 4, both Fe-single-doping and Ni-single-doping, as well as (Fe,Ni)-co-doping, increase the number of Fe-S and Ni-S bonds while reducing their bond lengths.

Table 3. Mulliken population analysis of atoms adjacent to Fe Ni impurity atoms.

Sample	Atom	s	p	d	Total	Charge/e
Cu ₂ ZnSnS ₄	Zn 1	0.42	0.94	9.98	11.34	0.66
	S 1, S 2, S 3, S 4	1.84	4.54	0	6.37	−0.37
	Cu 1	0.6	0.64	9.81	11.06	−0.06
Fe-doping Cu ₂ ZnSnS ₄	S 5, S 6, S 7, S 8	1.84	4.54	0	6.37	−0.37
	Fe 1	0.4	0.62	6.94	7.96	0.04
	S 1, S 2	1.83	4.41	0	6.24	−0.24
Ni-doping Cu ₂ ZnSnS ₄	S 3, S 4	1.83	4.43	0	6.26	−0.26
	Ni 1	0.5	0.69	8.84	10.03	−0.03
	S 1, S 2	1.83	4.45	0	6.29	−0.29
(Fe,Ni)-co-doping Cu ₂ ZnSnS ₄	S 3, S 4	1.83	4.45	0	6.28	−0.28
	Fe 1	0.41	0.62	6.91	7.94	0.06
	S 1, S 2, S 3	1.84	4.42	0	6.26	−0.26
	S 4	1.81	4.43	0	6.26	−0.26
	Ni 2	0.48	0.66	8.91	10.05	−0.05
	S 5, S 6	1.83	4.49	0	6.32	−0.32
	S 7, S 8	1.84	4.49	0	6.34	−0.34

Table 4. Mulliken population analysis of bonds adjacent to Fe Ni impurity atoms.

Sample	Bond	Population	Length (Å)
Cu ₂ ZnSnS ₄	S 1—Zn 1, S 2—Zn 1	0.40	2.3659
	S 3—Zn 1, S 4—Zn 1	0.41	2.3653
Fe-doping Cu ₂ ZnSnS ₄	S 1—Fe 1	0.64	2.1321
	S 2—Fe 1	0.64	2.1322
	S 3—Fe 1	0.60	2.1598
	S 4—Fe 1	0.60	2.1597
Ni-doping Cu ₂ ZnSnS ₄	S 3—Ni 1	0.49	2.2298
	S 4—Ni 1	0.49	2.2299
	S 1—Ni 1, S 2—Ni 1	0.50	2.2341
(Fe,Ni)-co-doping Cu ₂ ZnSnS ₄	S 1—Fe 1	0.64	2.1451
	S 2—Fe 1	0.64	2.1433
	S 3—Fe 1	0.58	2.1666
	S 4—Fe 1	0.58	2.1679
	S 5—Ni 2	0.47	2.2055
	S 6—Ni 2	0.47	2.2038
	S 7—Ni 2	0.48	2.2778
	S 8—Ni 2	0.48	2.2794

This effect can be attributed to the smaller ionic radius of Fe and Ni compared with Zn and Cu, which leads to lattice distortion in Cu₂ZnSnS₄ after doping and an enhanced electrostatic effect. The average population of S atoms adjacent to Fe and Ni after co-doping was 0.54, which was smaller than the average population of 0.56 observed after Fe-doping and Ni-doping. Furthermore, the average bond length of S atoms adjacent to Fe and Ni after co-doping was 2.2 Å, which was slightly longer than the average bond length of 2.19 Å observed after Fe-doping and Ni-doping. Hence, (Fe,Ni)-co-doping weakened the covalent bond in Cu₂ZnSnS₄ while increasing the bond length. Consequently, the lattice constant in the *c*-axis direction was distorted, and the cell volume increased slightly.

3.4. Optical Properties

This study investigated the effects of Fe and Ni-doping on the optical properties of Cu₂ZnSnS₄, including the complex dielectric function, absorption coefficient, reflectivity, and complex conductivity. The macroscopic optical properties of solids are typically described using the complex dielectric function $\epsilon(\omega) = \epsilon_1(\omega) + i\epsilon_2(\omega)$. Optical constants,

such as the complex dielectric function, absorption coefficient, reflectivity, and complex conductivity, were derived using the Kramer–Kronig (KK) transformation [45].

3.4.1. Complex Dielectric Function

The dielectric function is generally represented as a complex number, with the imaginary part providing valuable information about electronic transitions and band structures [48]. Figure 5 illustrates the complex dielectric function of Fe-doping and Ni-doping $\text{Cu}_2\text{ZnSnS}_4$, where Figure 5a displays the real part and Figure 5b shows the imaginary part. As illustrated in Figure 5a, the static dielectric constant of undoped $\text{Cu}_2\text{ZnSnS}_4$, denoted as $\epsilon_1(0) = 10.54$, was consistent with the findings in the literature [49]. Both Fe-single-doping and Ni-single-doping, as well as (Fe,Ni)-co-doping, led to an increase in the value of the static dielectric constant, $\epsilon_1(0)$. After co-doping, the static dielectric constant reached its maximum value of 100.49, which aligned with the results of the population analysis. Fe-doping and Ni-doping in $\text{Cu}_2\text{ZnSnS}_4$ introduce additional 3d electrons near the Fermi level. After doping, the covalent bond effect strengthened, leading to an intensified binding effect of the atomic nucleus charge, thus increasing the static dielectric constant. Figure 5b illustrates that the imaginary part, denoted as $\epsilon''(\omega)$, of the intrinsic $\text{Cu}_2\text{ZnSnS}_4$ complex dielectric function exhibited three distinct dielectric peaks at 1.39 eV, 3.84 eV, and 6.04 eV. In the density of states plot, the dielectric peak at 1.39 eV corresponded to the Cu-3d to Sn-5s orbital electron transition, the 3.84 eV peak corresponded to the Cu-3d to S-3p orbital electron transition, and the 6.04 eV peak corresponded to the Cu-3d to Sn-5p orbital electron transition. In the low-energy range of 0 to 2.5 eV, the $\text{Cu}_2\text{ZnSnS}_4$ dielectric peak shifted toward lower energies due to Fe-doping and Ni-doping in $\text{Cu}_2\text{ZnSnS}_4$. This shift occurred because Fe-doping and Ni-doping reduced the $\text{Cu}_2\text{ZnSnS}_4$ band gap, resulting in a redshift of the absorption peak. In the energy range of 2.5 to 10 eV, the dielectric peaks of Fe-doping and Ni-doping $\text{Cu}_2\text{ZnSnS}_4$ closely aligned with the intrinsic dielectric peak of $\text{Cu}_2\text{ZnSnS}_4$. These findings indicated that the dielectric properties of $\text{Cu}_2\text{ZnSnS}_4$ in the visible light range can be effectively controlled through Fe-doping, Ni-doping, or (Fe,Ni)-co-doping.

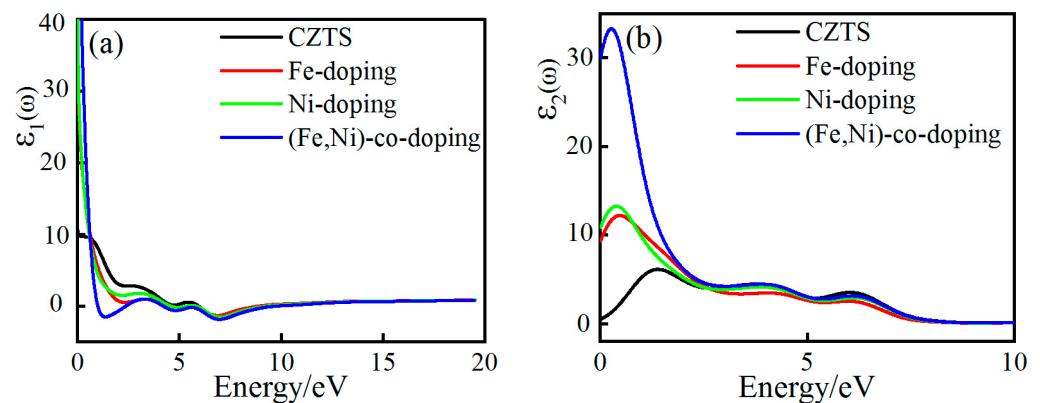


Figure 5. Fe-doping and Ni-doping $\text{Cu}_2\text{ZnSnS}_4$ complex dielectric function (a) Real part of the complex dielectric function (b) Imaginary part of the complex dielectric function.

3.4.2. Absorption and Reflection Spectra

Figure 6 illustrates the absorption coefficient and reflection spectrum of Fe-doping and Ni-doping $\text{Cu}_2\text{ZnSnS}_4$. As illustrated in Figure 6a, the absorption spectrum of $\text{Cu}_2\text{ZnSnS}_4$ can be divided into three regions: the visible light region spanning from 0.16 eV to 3.2 eV, the ultraviolet light absorption region ranging from 3.2 eV to 11 eV, and the high-energy absorption region beyond 11 eV. The absorption edge of $\text{Cu}_2\text{ZnSnS}_4$ was observed at 0.16 eV, corresponding to the calculated band gap. Fe-doping and Ni-doping $\text{Cu}_2\text{ZnSnS}_4$ exhibited a slight red shift in the absorption edge, which can be attributed to the reduction in the band gap following doping. In the energy range of 0.16 eV to 6.9 eV, the absorption coefficient gradually increased with the incident light energy and reached a maximum

value of $1.65 \times 10^5 \text{ cm}^{-1}$ at 6.9 eV. Beyond 6.9 eV, the absorption coefficient began to decrease and remained below 10^4 cm^{-1} after 11 eV. Notably, a significant absorption peak appeared at 1.9 eV with an absorption coefficient of $3.6 \times 10^4 \text{ cm}^{-1}$, indicating strong light absorption by $\text{Cu}_2\text{ZnSnS}_4$ in the visible light region [50]. The absorption coefficients of Fe-doped and Ni-doped $\text{Cu}_2\text{ZnSnS}_4$ in the visible light range all exceed 10^4 cm^{-1} . Among the three doping conditions, (Fe,Ni)-co-doping resulted in the highest absorption coefficient, followed by Fe-single-doping, while Ni-single-doping resulted in the lowest absorption coefficient, in line with the changes in the band gap resulting from Fe-doping and Ni-doping $\text{Cu}_2\text{ZnSnS}_4$. As illustrated in Figure 6b, $\text{Cu}_2\text{ZnSnS}_4$ primarily reflected light in the energy range of 7.4 eV to 9.4 eV, with reflectivity below 30% in the range of 1.5 eV to 6.3 eV. This indicated minimal reflection loss in the visible light range, thus favoring light absorption by $\text{Cu}_2\text{ZnSnS}_4$. In the visible light range, the reflectivity of Fe-doping and Ni-doping $\text{Cu}_2\text{ZnSnS}_4$ exhibited an increasing trend. Notably, (Fe,Ni)-co-doping resulted in the highest reflectivity, followed by Fe-single-doping, while Ni-single-doping yielded the lowest reflectivity. Thus, the absorption coefficient and reflectivity of $\text{Cu}_2\text{ZnSnS}_4$ can be effectively controlled through Fe-doping, Ni-doping, or (Fe,Ni)-co-doping.

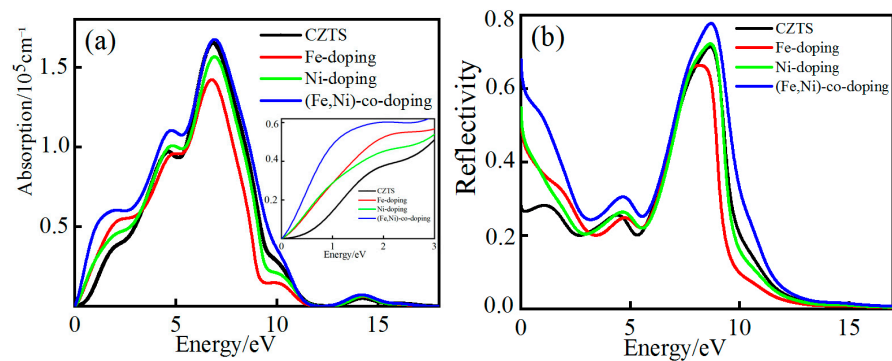


Figure 6. Absorption coefficient and reflection spectrum of Fe-doped and Ni-doped $\text{Cu}_2\text{ZnSnS}_4$. (a) Absorption coefficient. (b) Reflection spectrum.

3.4.3. Complex Conductivity

Figure 7 displays the complex conductivity of Fe-doped and Ni-doped $\text{Cu}_2\text{ZnSnS}_4$. As illustrated in Figure 7a, the conductivity decreased to nearly zero beyond an energy of 11.3 eV. In the energy range of 0 eV to 6.2 eV, three prominent peaks appeared, corresponding to the positions of the light absorption peaks. The primary peak observed at 1.9 eV indicated that $\text{Cu}_2\text{ZnSnS}_4$ possesses strong photoconductivity in the visible light range. Fe-doping and Ni-doping resulted in a slight shift of the peak position toward lower energies, accompanied by an increase in the peak magnitude. Among the three doping conditions, (Fe,Ni)-co-doping resulted in the most significant increase in the peak, followed by Fe-doping, while Ni-doping resulted in the smallest increase. These observations were consistent with the band gap changes in $\text{Cu}_2\text{ZnSnS}_4$ under the three doping conditions.

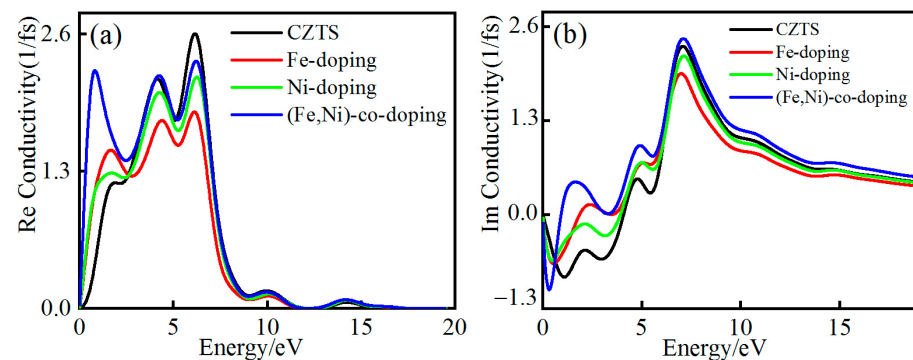


Figure 7. Complex conductivity of Fe-doped and Ni-doped $\text{Cu}_2\text{ZnSnS}_4$. (a) Real part. (b) Imaginary part.

4. Conclusions

In this study, the electronic structure and optical properties of Fe-doped, Ni-doped, and (Fe,Ni)-co-doped $\text{Cu}_2\text{ZnSnS}_4$ were calculated and analyzed using first-principles methods. The results indicated that Fe-doping and Ni-doping in $\text{Cu}_2\text{ZnSnS}_4$ weakened the charge transfer of adjacent S atoms, thereby enhancing the covalent bonding of Fe–S and Ni–S bonds, shortening bond lengths, and decreasing lattice constants a and c and the unit cell volume v . Fe-doping exhibited the highest formation energy, while Ni-doping had the lowest formation energy, with (Fe,Ni)-co-doping falling in the intermediate range. Both Fe and Ni-doping introduced 3d electrons near the Fermi level, resulting in an upward shift of the valence band and a downward shift of the conduction band, leading to a decrease in the $\text{Cu}_2\text{ZnSnS}_4$ band gap from 0.16 eV. (Fe,Ni)-co-doping had the most pronounced effect on the band gap. Both Fe and Ni-doping, as well as (Fe,Ni)-co-doping, increased the static dielectric constant of $\text{Cu}_2\text{ZnSnS}_4$, causing the dielectric peak to shift toward lower energy levels. In the visible light range, Fe-doping, Ni-doping, and (Fe,Ni)-co-doping resulted in increased light absorption with higher incident light energies, surpassing an absorption coefficient of 10^4 cm^{-1} . Notably, $\text{Cu}_2\text{ZnSnS}_4$ exhibited strong light absorption at 1.9 eV, with the highest absorption coefficient observed in the case of (Fe,Ni)-co-doping. Within the energy range of 1.5 eV to 6.3 eV, the reflectivity of $\text{Cu}_2\text{ZnSnS}_4$ doped with Fe, Ni, or both elements remained below 30%. Thus, $\text{Cu}_2\text{ZnSnS}_4$ possesses favorable photoconductivity in the visible light range. Furthermore, the introduction of Fe and Ni dopants resulted in a slight shift of the conductivity peak toward lower energy levels, accompanied by an overall increase in conductivity.

Author Contributions: Writing, X.Y.; experimental design, X.Y.; simulation calculation, X.Y.; analysis, X.Y.; writing—review and editing, X.Q.; model building, X.Q.; data analysis, W.Y.; overall planning, W.Y.; review and revision of the thesis, C.Z.; drawing, C.Z.; literature review, D.Z.; software, D.Z. All authors have read and agreed to the published version of the manuscript.

Funding: This research was funded by the Key Laboratory of Materials Simulation and Computing of Anshun University (Asxykpt201803) and the Youth Growth Project of Guizhou Provincial Department of Education, grant number KY (2020) 134.

Data Availability Statement: Not applicable.

Acknowledgments: This work was supported by the Youth Science and Technology Talent Growth Project of the Education Department of Guizhou Province (No.2020138), the Key Supporting Discipline of Materials and Aviation of Anshun College (2020), and the Guizhou Province JMRH Integrated Key Platform Funding Project.

Conflicts of Interest: The authors declare no conflict of interest.

References

1. Thirunavukkarasu, M.; Sawle, Y.; Lala, H. A comprehensive review on optimization of hybrid renewable energy systems using various optimization techniques. *Renew. Sustain. Energy Rev.* **2023**, *176*, 113192. [[CrossRef](#)]
2. Das, B.; Hossain, S.M.; Nandi, A.; Samanta, D.; Pramanick, A.K.; Chapa, S.O.M.; Ray, M. Spectral conversion by silicon nanocrystal dispersed gel glass: Efficiency enhancement of silicon solar cell. *J. Phys. D Appl. Phys.* **2021**, *55*, 025106. [[CrossRef](#)]
3. Okil, M.; Salem, M.S.; Abdolkader, T.M.; Shaker, A. From Crystalline to Low-cost Silicon-based Solar Cells: A Review. *Silicon* **2021**, *14*, 1895–1911. [[CrossRef](#)]
4. Koltsov, M.; Gopi, S.V.; Raadik, T.; Krustok, J.; Josepson, R.; Gržibovskis, R.; Vembris, A.; Spalatu, N. Development of Bi_2S_3 thin film solar cells by close-spaced sublimation and analysis of absorber bulk defects via in-depth photoluminescence analysis. *Sol. Energy Mater. Sol. Cells* **2023**, *254*, 112292. [[CrossRef](#)]
5. Eka, C.P.; Jessie, M.; Endi, S.; Andhy, S.; Ganes, S.; Mohammad, K.A.; Brian, Y. The effect of $\text{Cu}_{\text{Zn}}+\text{Zn}_{\text{Cu}}$ defect complex on $\text{Cu}_2\text{ZnSnS}_4$ thin film solar cell: A density functional theory study. *Mater. Chem. Phys.* **2023**, *296*, 127192.
6. Pan, B.; Wei, M.; Liu, W.; Jiang, G.; Zhu, C. Fabrication of $\text{Cu}_2\text{ZnSnS}_4$ absorber layers with adjustable Zn/Sn and Cu/Zn+Sn ratios. *J. Mater. Sci. Mater. Electron.* **2014**, *25*, 3344–3352. [[CrossRef](#)]
7. Su, Z.H.; Liang, G.X.; Fan, P.; Luo, J.; Zheng, Z.; Xie, Z.; Wang, W.; Chen, S.; Hu, J.; Wei, Y.; et al. Device Postannealing Enabling over 12% Efficient Solution-Processed $\text{Cu}_2\text{ZnSnS}_4$ Solar Cells with Cd^{2+} Substitution. *Adv. Mater.* **2020**, *32*, 2000121. [[CrossRef](#)]
8. Ki, W.; Hillhouse, H.W. Earth-Abundant Element Photovoltaics Directly from Soluble Precursors with High Yield Using a Non-Toxic Solvent. *Adv. Energy Mater.* **2011**, *1*, 732–735. [[CrossRef](#)]

9. Crovetto, A.; Hansen, O. What is the band alignment of $\text{Cu}_2\text{ZnSn}(\text{S},\text{Se})_4$ solar cells? *Sol. Energy Mater. Sol. Cells.* **2017**, *169*, 177–194. [[CrossRef](#)]
10. Bao, W.; Ichimura, M. Prediction of the Band Offsets at the $\text{CdS}/\text{Cu}_2\text{ZnSnS}_4$ Interface Based on the First-Principles Calculation. *Jpn. J. Appl. Phys.* **2012**, *51*, 10NC31. [[CrossRef](#)]
11. Chen, S.; Walsh, A.; Gong, X.G.; Wei, S.H. Classification of Lattice Defects in the kesterite $\text{Cu}_2\text{ZnSnS}_4$ and $\text{Cu}_2\text{ZnSnSe}_4$ Earth-Abundant Solar Cell Absorbers. *Adv. Mater.* **2013**, *25*, 1522–1539. [[CrossRef](#)] [[PubMed](#)]
12. Su, Z.; Tan, J.M.; Li, X.; Zeng, X.; Batabyal, S.K.; Wong, L.H. Cation Substitution of Solution-Processed $\text{Cu}_2\text{ZnSnS}_4$ Thin Film Solar Cell with over 9% Efficiency. *Adv. Energy Mater.* **2015**, *5*, 1500682. [[CrossRef](#)]
13. Choubac, L.; Bär, M.; Kozina, X.; Félix, R.; Wilks, R.G.; Brammertz, G.; Levchenko, S.; Arzel, L.; Barreau, N.; Harel, S.; et al. Sn Substitution by Ge: Strategies to Overcome the Open-Circuit Voltage Deficit of Kesterite Solar Cells. *ACS Appl. Energy Mater.* **2020**, *3*, 5830–5839. [[CrossRef](#)]
14. Zhou, J.Z.; Xu, X.; Duan, B.W.; Shi, J.J.; Luo, Y.H.; Wu, H.J.; Li, D.M.; Meng, Q.B. Research Progress of Metal(I) Substitution in $\text{Cu}_2\text{ZnSn}(\text{S},\text{Se})_4$ Thin Film Solar Cells. *Acta Chim. Sinica.* **2021**, *79*, 303–318. [[CrossRef](#)]
15. Neuschitzer, M.; Rodriguez, M.E.; Guc, M.; Marquez, J.A.; Giraldo, S.; Forbes, I.; Perez-Rodriguez, A.; Saucedo, E. Revealing the beneficial effects of Ge doping on $\text{Cu}_2\text{ZnSnSe}_4$ thin film solar cells. *J. Mater. Chem. A* **2018**, *6*, 11759. [[CrossRef](#)]
16. Yuan, Z.-K.; Chen, S.; Xiang, H.; Gong, X.-G.; Walsh, A.; Park, J.-S.; Repins, I.; Wei, S.-H. Engineering Solar Cell Absorbers by Exploring the Band Alignment and Defect Disparity: The Case of Cu- and Ag-Based Kesterite Compounds. *Adv. Funct. Mater.* **2015**, *25*, 6733–6743. [[CrossRef](#)]
17. Sravani, L.; Routray, S.; Courel, M.; Radhan, K.P. Loss mechanisms in CZTS and CZTSe kesterite thin-film solar cells: Understanding the complexity of defect density. *Sol. Energy.* **2021**, *227*, 56–66. [[CrossRef](#)]
18. Bencherif, H. Towards a high efficient Cd-free double CZTS layers kesterite solar cell using an optimized interface band alignment. *Sol. Energy* **2022**, *238*, 114–125. [[CrossRef](#)]
19. Kaur, K.; Nisika; Chowdhury, A.H.; Qiao, Q.; Kumar, M. Nanoscale charge transport and local surface potential distribution to probe the defect passivation in Cr-substituted earth abundant CZTS absorber layer. *J. Alloys Compd.* **2021**, *854*, 157160. [[CrossRef](#)]
20. Muska, K.; Timmo, K.; Pilvet, M.; Kaupmees, R.; Raadik, T.; Mikli, V.; Grossberg-Kuusk, M.; Krustok, J.; Josepson, R.; Lange, S.; et al. Impact of Li and K co-doping on the optoelectronic properties of CZTS monograin powder. *Sol. Energy Mater. Sol. Cells* **2023**, *252*, 112182. [[CrossRef](#)]
21. Liu, B.; Guo, J.; Hao, R.; Wang, L.; Gu, K.; Sun, S.; Aierken, A. Effect of Na doping on the performance and the band alignment of CZTS/CdS thin film solar cell. *Sol. Energy.* **2020**, *201*, 219–226. [[CrossRef](#)]
22. Heydar, H.N.; Tara, P.D. Influence of Ag-doping on the performance of $\text{Cu}_2\text{ZnSnS}_4$ solar cells. *Sol. Energy.* **2023**, *253*, 321–331.
23. Ashfaq, A.; Jacob, J.; Amami, M.; Al-Harbi, F.; Ali, A.; Mahmood, K.; Rehman, U.; Amin, N.; Ikram, S.; Akbar, S.T.; et al. Effect of Al-doping on the thermoelectric properties of CZTS thin film grown by sol-gel method. *Solid State Commun.* **2022**, *345*, 114701. [[CrossRef](#)]
24. Pandey, A.; Yadav, P.; Kumar, P.; Singh, M.K. Synthesis, morphological and optical properties of hydrothermally synthesized Bi and Mn co-doped $\text{Cu}_2\text{ZnSnS}_4$ (CZTS). *Mater. Today Proc.* **2022**, *11*, 407. [[CrossRef](#)]
25. Gupta, A.K.S.; Farhad, S.F.U.; Habib, S.; Hossain, M.R.; Hossain, K.; Das, N.K.; Quamruzzaman, M.; Matin, M.; Amin, N. Characterizations of extrinsically doped CZTS thin films for solar cell absorbers fabricated by sol-gel spin coating method. *Appl. Surf. Sci. Adv.* **2023**, *13*, 100352. [[CrossRef](#)]
26. Liang, X.; Zhang, D.; Wu, Z.; Wang, D. The Fe-promoted MoP catalyst with high activity for water splitting. *Appl. Catal. A Gen.* **2016**, *524*, 134–138. [[CrossRef](#)]
27. Hohenberg, P.; Kohn, W. Inhomogeneous Electron Gas. *Phys. Rev.* **1964**, *136*, B864–B871. [[CrossRef](#)]
28. Kohn, W.; Sham, L.J. Self-consistent Equations Including Exchange and Correlation Effects. *Phys. Rev.* **1965**, *140*, A1133–A1138. [[CrossRef](#)]
29. Ismael, M. One-step ultrasonic-assisted synthesis of Ni-doped g-C₃N₄ photocatalyst for enhanced photocatalytic hydrogen evolution. *Inorg. Chem. Commun.* **2023**, *151*, 110607. [[CrossRef](#)]
30. Schorr, S.; Hoebler, H.-J.; Tovar, M. A neutron diffraction study of the stannite-kesterite solid solution series. *Eur. J. Miner.* **2007**, *19*, 65–73. [[CrossRef](#)]
31. Segall, M.D.; Lindan, P.; Probert, M.J.; Pickard, C.J.; Hasnip, P.J.; Clark, S.J.; Payne, M.C. First-principles simulation: Ideas, illustrations and the CASTEP code. *J. Phys. Condens. Matter* **2002**, *14*, 2717–2744. [[CrossRef](#)]
32. Clark, S.J.; Segall, M.D.; Pickard, C.J.; Hasnip, P.J.; Probert, M.I.J.; Refson, K.; Payne, M.C. First principles methods using CASTEP. *Z. Kristallogr. Cryst. Mater.* **2005**, *220*, 567–570. [[CrossRef](#)]
33. Perdew, J.P.; Burke, K.; Ernzerhof, M. Generalized Gradient Approximation Made Simple. *Phys. Rev. Lett.* **1996**, *77*, 3865–3868. [[CrossRef](#)]
34. Vanderbilt, D. Soft self-consistent pseudopotentials in a generalized eigenvalue formalism. *Phys. Rev. B.* **1990**, *41*, 7892–7895. [[CrossRef](#)] [[PubMed](#)]
35. Li, M.; Zhang, J.; Zhang, Y. First-principles calculation of compensated (2N, W) codoping impacts on band gap engineering in anatase TiO_2 . *Chem. Phys. Lett.* **2012**, *527*, 63–66. [[CrossRef](#)]

36. Long, R.; English, N.J. Synergistic Effects of Bi/S Codoping on Visible Light-Activated Anatase TiO₂ Photocatalysts from First Principles. *J. Phys. Chem. C* **2009**, *113*, 8373–8377. [[CrossRef](#)]
37. Paier, J.; Asahi, R.; Nagoya, A.; Kresse, G. Cu₂ZnSnS₄ as a potential photovoltaic material: A hybrid Hartree-Fockdensity functional theory study. *Phys. Rev. B* **2009**, *79*, 115126. [[CrossRef](#)]
38. Sun, D.; Ding, Y.; Kong, L.; Zhang, Y.; Guo, X.; Wei, L.; Zhang, L.; Zhang, L. First-principles Study on Mg Doping in Cu₂ZnSnS₄. *J. Inorg. Mater.* **2020**, *35*, 1290–1294. [[CrossRef](#)]
39. Digraaskar, R.V.; Mali, S.M.; Tayade, S.B.; Ghule, A.V.; Sathe, B.R. Overall noble metal free Ni and Fe doped Cu₂ZnSnS₄ (CZTS) bifunctional electrocatalytic systems for enhanced water splitting reactions. *Int. J. Hydrogen Energy* **2019**, *44*, 8144–8155. [[CrossRef](#)]
40. Liu, X.; Zhong, Q.; Guo, W.; Zhang, W.; Ya, Y.; Xia, Y. Novel Platycladus orientalis-shaped Fe-doped ZnO hierarchical nanoflower-decorated with Ag nanoparticles for photocatalytic application. *J. Alloys Compd.* **2021**, *880*, 160501. [[CrossRef](#)]
41. Mo, M.; Zeng, J.-S.; He, H.; Zhang, L.; Du, L.; Fang, Z.-J. The first-principle study on the formation energies of Be, Mg and Mn doped CuInO₂. *Acta Phys. Sin.* **2019**, *68*, 106102. [[CrossRef](#)]
42. Zhao, H.; Persson, C. Optical properties of Cu(In,Ga)Se₂ and Cu₂ZnSn(S,Se)₄. *Thin Solid Film.* **2011**, *519*, 7508–7512. [[CrossRef](#)]
43. Islam, S.; Majumdar, P.; Hossain, M.A.; Ahmed, F. Effect of Fe³⁺ Doping concentration in Cu₂ZnSnS₄ thin film: Structural and Optical Analysis. *J. Mater. Sci. Eng. A.* **2022**, *12*, 97–106.
44. Chen, H.J.; Fu, S.W.; Wu, S.H.; Tsai, T.C.; Wu, H.T.; Shih, C.F. Structural and photoelectron spectroscopic studies of band alignment at the Cu₂ZnSnS₄/CdS heterojunction with slight Ni doping in Cu₂ZnSnS₄. *J. Phys. D Appl. Phys.* **2016**, *49*, 335102. [[CrossRef](#)]
45. Lebègue, S.; Arnaud, B.; Alouani, M. Calculated quasiparticle and optical properties of orthorhombic and cubic Ca₂Si. *Phys. Rev. B.* **2005**, *72*, 085103. [[CrossRef](#)]
46. Borlido, P.; Schmidt, J.; Huran, A.W.; Tran, F.; Marques, M.A.L.; Botti, S. Exchange-correlation functionals for band gaps of solids: Benchmark, reparametrization and machine learning. *NPJ Comput. Mater.* **2020**, *6*, 96. [[CrossRef](#)]
47. Xiao, C.; Li, K.; Zhang, J.; Tong, W.; Liu, Y.; Li, Z.; Huang, P.; Pan, B.; Su, H.; Xie, Y. Magnetic ions in wide band gap semiconductor nanocrystals for optimized thermoelectric properties. *Mater. Horizons.* **2014**, *1*, 81–86. [[CrossRef](#)]
48. Prokopidis, K.; Kalialakis, C. Physical interpretation of a modified Lorentz dielectric function for metals based on the Lorentz–Diracforce. *Appl. Phys. B* **2014**, *117*, 25–32. [[CrossRef](#)]
49. Li, C.R.; Li, Y.F.; Yao, B.; Yang, G.; Zhan, H.D.; Deng, R.; Liu, L. Electronic and optical properties of kesterite Cu₂ZnSnS₄ under in-plane biaxial strains: First-principles calculations. *Phys. Lett. A* **2013**, *377*, 2398–2402. [[CrossRef](#)]
50. Behera, N.; Mohan, D.B. Investigation of broad-band optical absorption and electrical properties in vacuum annealed CZTS/Ag multi-layered stack structure for plasmonic solar cell application. *Opt. Mater.* **2022**, *127*, 112316. [[CrossRef](#)]

Disclaimer/Publisher’s Note: The statements, opinions and data contained in all publications are solely those of the individual author(s) and contributor(s) and not of MDPI and/or the editor(s). MDPI and/or the editor(s) disclaim responsibility for any injury to people or property resulting from any ideas, methods, instructions or products referred to in the content.